

## Photocatalytic removal of the erythromycin antibiotic using Fe-doped $\text{TiO}_2@Fe_3O_4$ magnetic nanoparticles: investigation of effective parameters, process kinetics and degradation end products

Hassan Pishrafti<sup>a</sup>, Hossein Kamani<sup>b\*</sup>, Nabiollah Mansouri<sup>a</sup>, Amir Hessam Hassani<sup>a</sup>, Homayon Ahmadpanahi<sup>c</sup>

<sup>a</sup>Faculty of Natural Resources and Environment, Department of Environmental Engineering, Science and Research Branch, Islamic Azad University, Tehran, Iran, emails: pishrafti@yahoo.com (H. Pishrafti), nmansourin@gmail.com (N. Mansouri), ahassani@srbiau.ac.ir (A.H. Hassani)

<sup>b</sup>Health Promotion Research Center, Zahedan University of Medical Sciences, Zahedan, Iran, Tel. +989155412919; Fax +98 5433295837; email: hossein\_kamani@yahoo.com

<sup>c</sup>Chemistry Department, Central Tehran Branch, Islamic Azad University, Tehran, Iran, email: H.ahmadpanahi@iauctb.ac.ir

Received 8 December 2021; Accepted 14 April 2022

### ABSTRACT

Antibiotics are resistant compounds with low biodegradability and cannot be effectively eliminated by conventional wastewater treatment methods. The aim of this study was to evaluate the photocatalytic removal of erythromycin using magnetic nanoparticles (Fe-doped  $\text{TiO}_2@Fe_3O_4$ ) from aqueous solutions. Fe-doped  $\text{TiO}_2@Fe_3O_4$  nanoparticles were synthesized by sol-gel method, and scanning electron microscopy, energy-dispersive X-ray spectroscopy, Fourier-transform infrared spectroscopy, X-ray diffraction, value-stream mapping, Brunauer–Emmett–Teller, and diffuse reflectance spectroscopy analyses were used to determine the properties of the synthesized nanoparticles. Effect of various variables including pH (3–9), initial concentration of erythromycin (25–75 mg/L), and concentration of nanoparticles (200–600 mg/L) at different times (15–60 min) was examined in the photocatalytic removal of erythromycin. The results of this study showed that the highest removal efficiency of erythromycin and the highest reaction rate constant were obtained using a fixed beam with a UVC lamp 15 W at pH = 5, the initial concentration of 25 mg/L, and the dose of nanoparticles 600 mg/L at the reaction time of 60 min. Due to the high removal efficiency of erythromycin by Fe-doped  $\text{TiO}_2@Fe_3O_4$  process in the presence of UVC light and stability of nanoparticles after 5 reuse, the application of this process in water and wastewater treatment processes is recommended.

**Keywords:** Fe-doped  $\text{TiO}_2@Fe_3O_4$ ; Photocatalytic process; Erythromycin antibiotic; Reaction products

### 1. Introduction

Antibiotics are widely used as human and animal drugs to treat microbial infections [1,2]. About 30%–90% of antibiotics are not broken down in humans and animals and enter the environment as active compounds from urine and

feces [3]. Some of the adverse effects of antibiotics include increased bacterial resistance, genotoxicity, and gastrointestinal disorders [4,5]. Erythromycin (C<sub>37</sub>H<sub>67</sub>NO<sub>13</sub>) is a macrolide antibiotic that has prokinetic activity in low doses [6]. The use of low-dose of erythromycin for a long time has

\*Corresponding author

This article was originally published with errors in affiliation 'a'. This version has been updated. Please see Corrigendum in vol. 295 (2023) 255 (doi: 10.5004/dwt.2023.29752)

been effective in the treatment of diffuse bronchiolitis [7]. Discharge of the antibiotic into the environment without proper treatment can cause widespread problems such as heart disorders, allergic and gastrointestinal reactions for humans and the ecosystem. Therefore, removal and reduction of erythromycin concentration before discharge to the environment are necessary and inevitable. So far, various methods including membrane processes [8], adsorption [2], and advanced oxidation processes including, ozonation [9], UV, and combined methods such as photo-Fenton [10], electro-Fenton [11],  $\text{Bi}_2\text{O}_3/\text{TS-1}$  [12], biopolymers [13], POM/polymer photocatalyst [14], and nanosheets [15] have been used by researchers to remove antibiotics. Among the above methods, the advanced oxidation process is an excellent and effective method for the degradation of hazardous, resistant, and non-degradable pollutants from aqueous solutions [16]. The advantages of the advanced oxidation process include process simplicity, low cost, high efficiency, and mineralization of pollutants [17]. The photocatalytic process is defined as the degradation of pollutants using light in the presence of an accelerating catalyst [18]. The use of catalysts in the presence of UV increases the reaction speed, reduces the time required, increases the production of hydroxyl radicals, reduces the production of toxic products, and increases efficiency [19].

Shang et al. [12] performed a study of photocatalytic analysis of erythromycin using  $\text{Bi}_2\text{O}_3/\text{TS-1}$  based on an artificial neural network. The results of the study showed that the highest removal efficiency of erythromycin (98.02%) under optimal conditions  $\text{Bi} = 5.5\%$  and the amount of catalyst was 600 mg/L [12].

Various materials such as biopolymers, zeolites, bio-cides, activated carbon, titanium dioxide, zinc oxide, etc. have been used to decompose drugs in aqueous solutions [13,20,21].

One of the most well-known catalysts used in the treatment of antibiotics from aqueous media is titanium dioxide ( $\text{TiO}_2$ ). However, the application of titanium dioxide is limited due to the wide bandgap (3.2 electron volts), low quantum efficiency, and hole/electron recombination [22]. To solve this problem, the researchers have been proposed  $\text{TiO}_2$  doping with metal ions (such as Mn, Ni, Zn, Ag, Au, Pt, Fe, etc.), or non-metallic (such as boron (B), nitrogen (N)), sensitization with dyes, sensitization with polymers, and formation of heterogeneity with other semiconductors [23]. Studies over the past decade have shown that, among the above methods, the doping of titanium dioxide with metal ions has shown better results in the removal of various contaminants. In the method of doping with metal ions,  $\text{Fe}^{3+}$  due to the half-full electron arrangement and high similarity of  $\text{Fe}^{3+}$  ion radius (0.645 Å) to  $\text{Ti}^{4+}$  (0.604 Å) and easy connection to the crystal lattice of titanium dioxide has been considered as an appropriate element [24,25].

There are various methods for preparation of nanoparticles, including hydrothermal, sol-gel, plasma oxidative pyrolysis, flame spray pyrolysis, precipitation, co-precipitation, immersion and wet impregnation. Among them, the sol-gel method is widely used. Compared to other methods of nanoparticle production, sol-gel has many advantages. Ability to cover large and complex surfaces [26–29].

After synthesis of an effective catalyst in removing various contaminants, separation and reuse of the catalyst are

very important and inevitable. This process is usually done with the help of filtration and centrifugation processes, which is associated with the consumption of a lot of time, money, and manpower. Therefore, to solve this problem, in the present study, the induction of magnetic properties to the catalyst (with iron oxide nanoparticles ( $\text{Fe}_3\text{O}_4$  NPs)) and their separation by an external magnet was used. In view of the foregoing, the purpose of the present study can be summarized as follows:

- Synthesis of Fe-doped  $\text{TiO}_2@/\text{Fe}_3\text{O}_4$  magnetic nanoparticles by sol-gel method and investigation of its physical and chemical properties.
- Investigation of ability of synthesized catalyst in the removal of erythromycin antibiotic and determination of the effect of different process parameters on the removal rate.
- Investigation of process kinetics.
- Checking the reusability of the adsorbent.
- Determining the final products resulting from the degradation of the antibiotic erythromycin.

## 2. Materials and methods

### 2.1. Materials used

In this study, erythromycin produced by Sigma-Aldrich Company was used to prepare a stock solution. Other chemicals used include tetraisopropyl orthotitanate ( $\text{C}_{12}\text{H}_{28}\text{O}_4\text{Ti}$ , 98%), nitric acid ( $\text{HNO}_3$ , 65%), iron(III) nitrate nonahydrate ( $\text{Fe}(\text{NO}_3)_3 \cdot 9\text{H}_2\text{O}$ ,  $\geq 98\%$ ), 2-propanol ( $\text{CH}_3\text{CH}(\text{OH})\text{CH}_3$ ), ammonia, iron chloride ( $\text{FeCl}_2$ ), ferric chloride ( $\text{FeCl}_3$ ), sulfuric acid ( $\text{H}_2\text{SO}_4$ , 95%–97%), and sodium hydroxide ( $\text{NaOH}$ , 98%) were purchased from Merck Co., Germany.

### 2.2. Synthesis of iron oxide ( $\text{Fe}_3\text{O}_4$ ) magnetic nanoparticles

In the present study, the co-precipitation method was used to synthesize magnetic nanoparticles. For this purpose, 2 and 5.12 g of  $\text{FeCl}_2$  and  $\text{FeCl}_3$  were added to 200 mL of distilled water in a balloon, respectively. The mixture was stirred at 600 rpm. Then, 1.5 M ammonia was added dropwise to the solution. After reaching the pH above 9, the addition of ammonia was stopped. The result of this reaction was the formation of a black precipitate in the solution. It should be noted that nitrogenation and stirring of the solution continued for up to 2 h after the addition of ammonia. After completion of the reaction, the obtained nanoparticles were washed several times with double distilled water and dried at ambient temperature [30].

### 2.3. Synthesis of Fe-doped $\text{TiO}_2@/\text{Fe}_3\text{O}_4$ nanoparticles

In this study, the sol-gel method was used to synthesize Fe-doped  $\text{TiO}_2$  and Fe-doped  $\text{TiO}_2@/\text{Fe}_3\text{O}_4$  catalysts. To prepare the samples, a certain amount of iron nitrate, 2-propanol alcohol, deionized water, and nitric acid was poured into a flat bottom balloon and stirred on a magnetic stirrer for 15 min until thoroughly mixed (Solution No. 1). In another Erlenmeyer flask, a certain amount of tetraisopropyl orthotitanate, 2-propanol, and  $\text{Fe}_3\text{O}_4$  were mixed

with a stirrer to form a uniform solution (Solution No. 2). Solution No. 1 was then added dropwise to the solution of mixing vessel No. 2. After 30 min of mixing both the solution and the formation of the sol, the balloon containing sol was placed in the laboratory at room temperature for 5 h to form a gel with high strength and adhesion. The resulting gel was dried in the oven for 24 h at 80°C and then the resulting dry powder was calcined in the oven for 1 h at 500°C after washing several times with distilled water. Scanning electron microscopy (SEM), energy-dispersive X-ray spectroscopy (EDX), Fourier-transform infrared spectroscopy (FTIR), X-ray diffraction (XRD), value-stream mapping (VSM), Brunauer–Emmett–Teller (BET), and diffuse reflectance spectroscopy (DRS) analyses were performed to characterize the synthesized nanoparticles [29].

#### 2.4. Photocatalytic degradation process of erythromycin

The present study was an experimental study with an applied approach on a laboratory scale that was performed in a batch system. At this stage, the effect of various variables such as the concentration of pollutants, the concentration of Fe-doped  $\text{TiO}_2@Fe_3O_4$  magnetic nanoparticles, the time of UV exposure, and the initial pH of the solution was studied on the efficiency of the degradation process. For the photodegradation of antibiotics, a 15-W UV-C UV lamp was used. For conducting the experiments, the desired concentrations of erythromycin (25, 50, and 75 mg/L) were prepared by diluting a certain amount of erythromycin stock solution in a volume of 250 mL. The pH of the solution was adjusted in the range 3, 5, 7, and 9 using 0.1 N sodium hydroxide and sulfuric acid and then a certain amount of magnetic catalyst of titanium dioxide doped with iron (200, 400, and 600 mg/L) was added to the solution. Sampling was performed at 15–60 min at different intervals of the irradiated suspension. After separating the nanoparticles from the process solution, the amount of light absorbed by the residual contaminant was read using a spectrophotometer at a specified wavelength and the antibiotic concentration in the solution was determined based on a calibration diagram.

### 3. Results and discussion

#### 3.1. Evaluation of the catalyst properties

##### 3.1.1. SEM analysis

Fig. 1a–c show the images of  $Fe_3O_4$ , Fe-doped  $TiO_2$ , and Fe-doped  $TiO_2@Fe_3O_4$  catalysts, respectively. The surface morphology of the nanoparticles shows that the synthesized samples are not clearly different from each other and tend to aggregate and agglomerate in all samples. This property can be due to the magnetic properties and fineness of these nanoparticles [31].

##### 3.1.2. EDX analysis

Fig. 2a–c show the EDX spectrum diagrams for  $Fe_3O_4$ , Fe-doped  $TiO_2$  and Fe-doped  $TiO_2@Fe_3O_4$  nanoparticles, respectively. As shown in the figures, the spectrum of the participating elements confirms the presence of Ti, Fe, and

O elements in the structure of the synthesized samples. The mass percentage of elements in the synthesized samples was calculated using EDX analysis and is presented in Table 1. The results of Table 1 show the presence of the above elements in the structure of synthesized nanocatalysts and also confirm the doping process of synthesized nanoparticles. In addition, the absence of other elements in the EDX analysis spectrum confirms the absence of impurities in the structure of the synthesized nanocatalysts. Strong Ti and O signals in the EDX spectrum indicate that  $TiO_2$  surrounds  $Fe_3O_4$  with a core-shell structure.

##### 3.1.3. FTIR analysis

The results of FTIR analysis of the nanoparticles synthesized in this study are shown in Fig. 3. As shown in the figure, the peak at  $585\text{ cm}^{-1}$  for  $Fe_3O_4$  nanoparticles indicates the vibrational stretching bond of Fe–O [32] while for the Fe– $TiO_2$  and Fe– $TiO_2@Fe_3O_4$  samples, peaks in the range of  $1,450\text{--}645\text{ cm}^{-1}$  can be attributed to Ti–O and Ti–O–Ti [33]. The small peaks in  $1,615$  and  $1,628\text{ cm}^{-1}$  can be attributed to O–H bending bond vibrations caused by the decomposition of water molecules or adsorbed water molecules. Peaks in the range of  $3,230\text{--}3,440\text{ cm}^{-1}$  specify the stretching vibrations of the hydroxyl group (structural hydroxyl and OH water group) [34]. The higher intensity of these two peaks in Fe– $TiO_2@Fe_3O_4$  sample signposts the presence of more hydroxyl and water groups adsorbed on the surface of Fe– $TiO_2@Fe_3O_4$ , which increase the production of hydroxyl radicals during the photocatalytic treatment process and consequently increase the photocatalytic activity of sample [35,36]. The presence of radicals on the surface of catalysts during the photocatalytic process plays an effective role in the process of degradation and removal of contaminants. This event that the water adsorbed on the catalyst surface increases the oxidation power of the photocatalytic system has been proven by other studies. The hydroxyl group on the surface of the catalyst can react with the optical cavities created and produce reactive oxygen species. In addition, such hydroxyls prolong the charge separation in the catalysts and delay the electron/hole recombination, which ultimately leads to increased activity of photocatalytic processes [37]. According to the study of Craciun et al. [34], a slight shift in the position of the peaks for the doped sample can be attributed to the replacement of  $Fe^{3+}$  in the titanium dioxide network or non-crystalline iron oxides at the boundary of the titanium dioxide crystals.

##### 3.1.4. XRD analysis

In order to determine the crystal structure and estimate the size of the formed crystals and to determine the phase of the crystal structure of nanoparticles, X-ray diffraction (XRD) spectroscopy with a wavelength of  $1.5418\text{ \AA}$  was used. Fig. 4 shows the XRD spectrum of Fe-doped  $TiO_2$  and Fe-doped  $TiO_2@Fe_3O_4$  nanoparticles at a  $2\theta$  of  $10^\circ\text{--}80^\circ$ .

As shown in Fig. 4, the XRD spectra of synthesized titanium dioxide samples have large and sharp peaks that indicate good crystal structure in the synthesized nanoparticles. Peaks at  $25.32$ ,  $37.78$ ,  $47.98$ ,  $54.20$ ,  $55.02$ ,  $62.11$ ,  $69.21$ ,

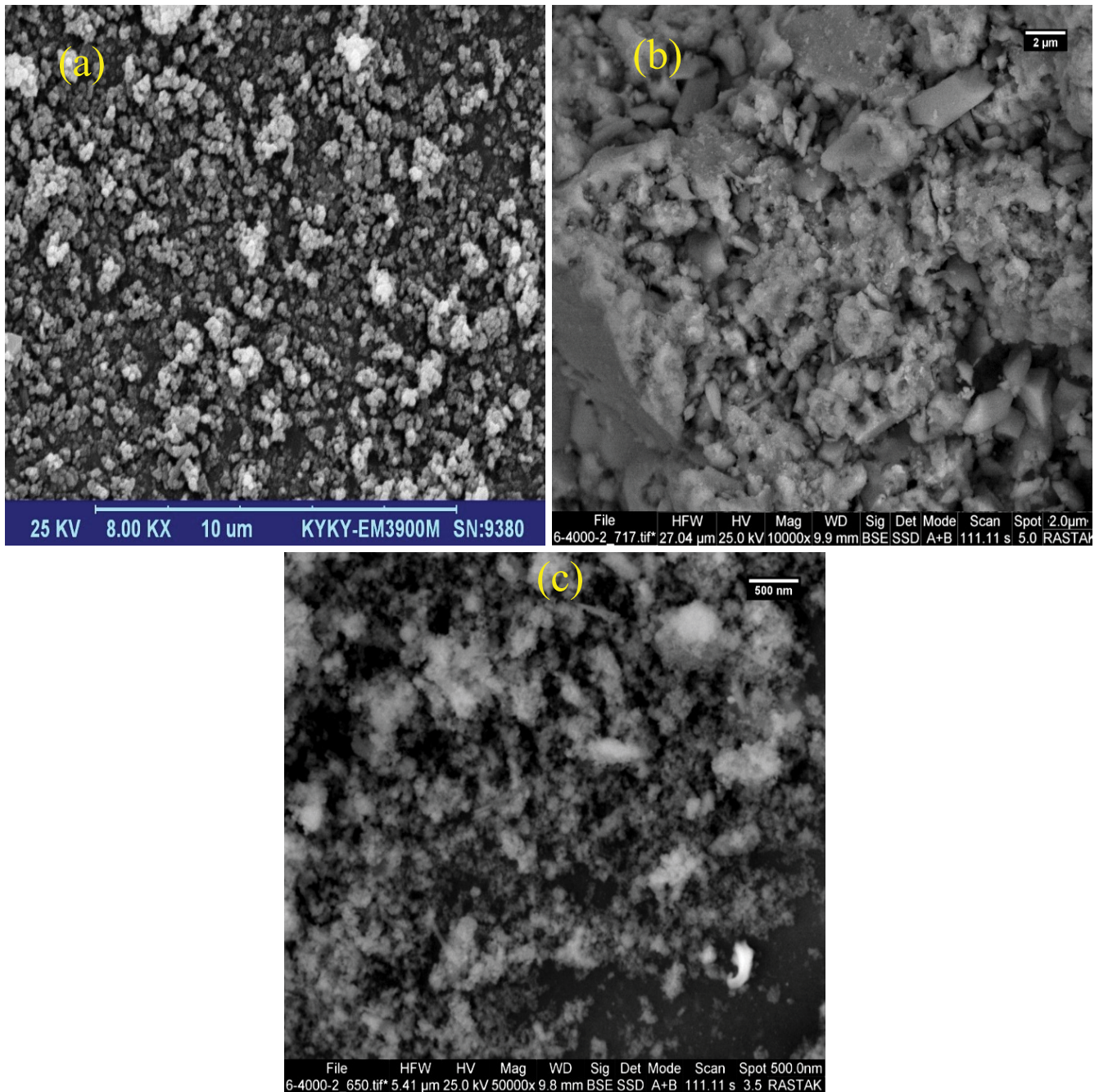


Fig. 1. SEM images of (a)  $\text{Fe}_3\text{O}_4$ , (b) Fe-doped  $\text{TiO}_2$  and (c) Fe-doped  $\text{TiO}_2@ \text{Fe}_3\text{O}_4$  nanoparticles.

70.48, and 75.23 which are specified in the Fe- $\text{TiO}_2$  sample approve crystal structure of anatase phase. Choi et al. [38] studied the effect of different doping agents on the phase transition from anatase to rutile and showed that the addition of small-radius doping agent could be integrated directly with the titanium dioxide crystal lattice to increase the anatase phase, which has more photocatalytic properties compared to other phases. As shown in Fig. 4, no peak of iron element was observed in iron-doped nanoparticles, which confirms that the crystal structure of  $\text{TiO}_2$  has not changed significantly. Eadi et al. [39] also reported that the

absence of a significant peak after the doping process could be due to the amount of iron doped lower than the limit of detection of device. On the other hand, occupation of a number of titanium dioxide lattice sites by iron ions is possible due to the similarity of the ionic radii of  $\text{Ti}^{4+}$  (0.604 Å) and  $\text{Fe}^{3+}$  (0.645 Å) [24].

Rahul Reddy et al. [40] showed that the replacement of iron in the crystalline lattice of titanium dioxide can lead to a reduction in the rutile phase, which in turn can be due to the reduction of oxygen sites on the surface of titanium dioxide; this prevents the crystallization of other

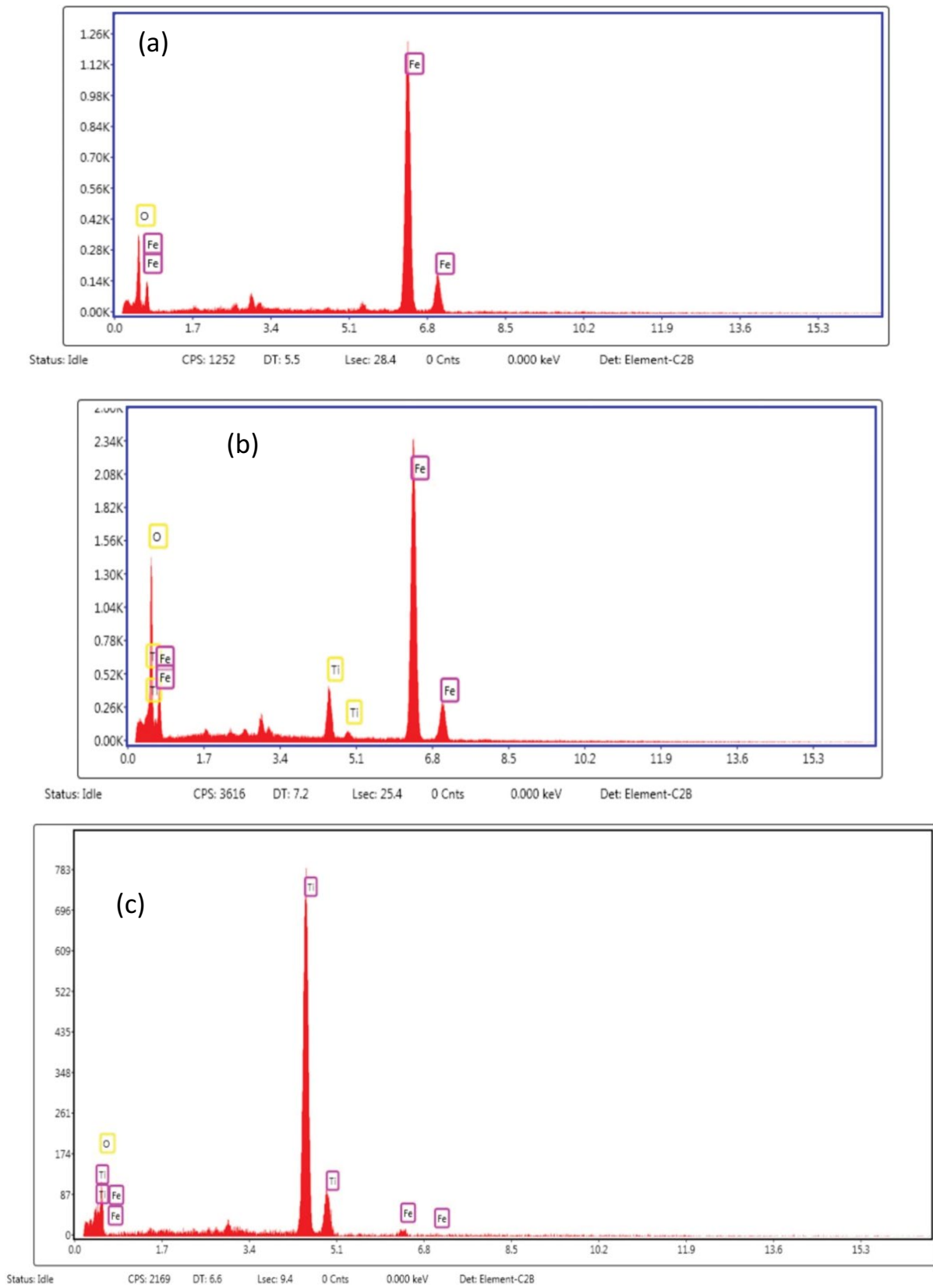


Fig. 2. EDX spectra for (a)  $\text{Fe}_3\text{O}_4$ , (b) Fe-doped  $\text{TiO}_2$  and (c) Fe-doped  $\text{TiO}_2@Fe_3\text{O}_4$  particles.

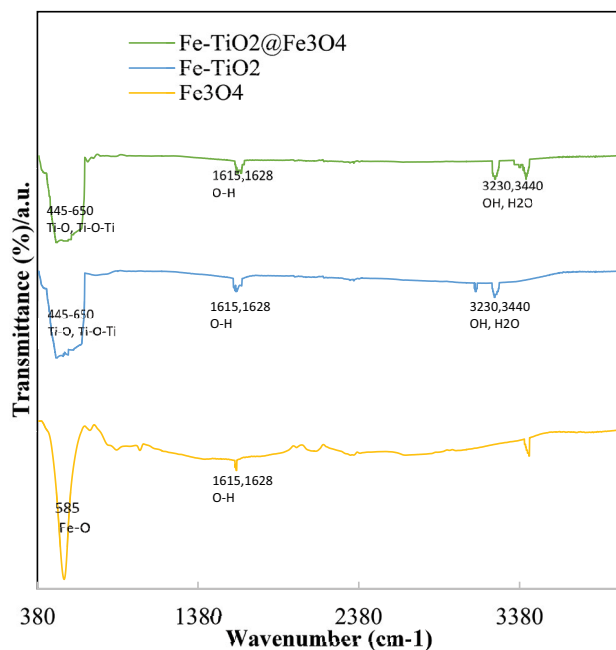


Fig. 3. FTIR spectra of  $\text{Fe}_3\text{O}_4$ , Fe-doped  $\text{TiO}_2$  and Fe-doped  $\text{TiO}_2@Fe_3\text{O}_4$  nanoparticles.

phases. On the other hand, an increase in the amount of iron can lead to changes in reflections at lower angles due to the replacement of  $\text{Ti}^{4+}$  ions with slightly larger  $\text{Fe}^{3+}$  ions [41]. According to the diagram of  $\text{Fe}_3\text{O}_4$  nanoparticles, the diffraction peaks at 30.16, 35.36, 43.43, 57.54, 56.92, and 62.51 can be related to the diffraction of the face-centered cubic. Also, in the diagram of  $\text{Fe-TiO}_2@Fe_3\text{O}_4$ , peaks related to  $\text{Fe-TiO}_2$  and  $\text{Fe}_3\text{O}_4$  are observed, which confirms the presence of  $\text{Fe}_3\text{O}_4$  and  $\text{Fe-TiO}_2$  in the structure of  $\text{Fe-TiO}_2@Fe_3\text{O}_4$ .

The calculation of crystallite size of the synthesized samples was performed using the Debye–Scherrer equation and based on the following formula:

$$D = \frac{K}{\beta \cos\theta} \quad (1)$$

where the average diameter of the crystallite size (nanometers) was shown by  $D$ ,  $K$  represents crystal shape factor (it is typically constant and equal to 0.9),  $\lambda$  is indicative of X-ray wavelength, which is employed for XRD analysis (the wavelength was 1.5441 Å in the present study),  $\theta$  is used for representing diffraction angle in terms of degree, and  $\beta$  is representative of the full-width at half maximum (FWHM). Accordingly, the average size of  $\text{Fe-TiO}_2$  and  $\text{Fe}_3\text{O}_4$  nanoparticles were 15.05 and 18.12 nm, respectively.

### 3.1.5. DRS analysis

DRS analysis has been used to evaluate the reduction in bandgap size after doping of elements doped in the structure of synthesized nanoparticles. Fig. 5 shows the absorption spectra of two synthesized samples in the wavelength range of 300–800 nm. In addition to determining the absorption spectrum, it is possible to quantify the band

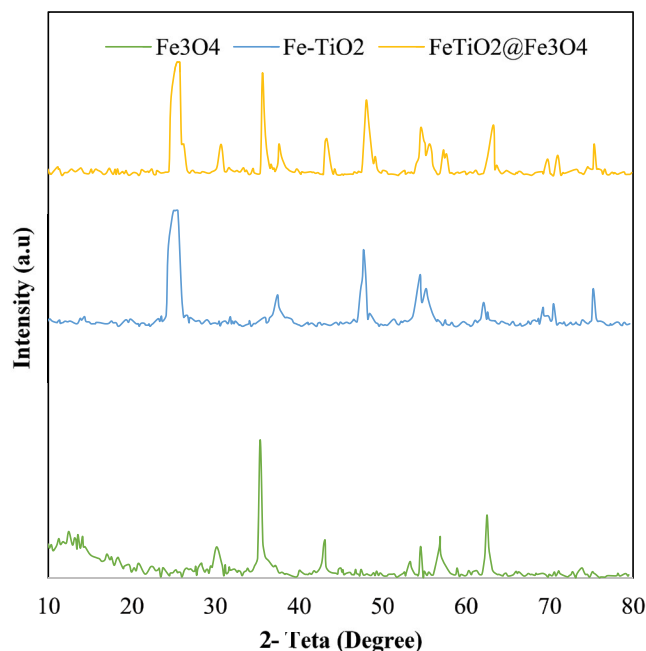


Fig. 4. XRD spectrum of  $\text{Fe}_3\text{O}_4$ , Fe-doped  $\text{TiO}_2$  and Fe-doped  $\text{TiO}_2@Fe_3\text{O}_4$  nanoparticles.

gap of nanoparticles using DRS analysis data and using the Kubelka–Munk function and the Tauc method followed by plotting  $ah\nu^{1/2}$  against the energy of absorbed photons in terms of electron volts (eV).

$$(ah\nu) = A(h\nu - E_g)^r \quad (2)$$

where  $a$  indicates the absorption coefficient,  $h$  signifies the Planck's constant,  $\nu$  shows the light frequency,  $A$  represents the absorption constant,  $E_g$  is indicative of the nanoparticle bandgap, and  $r$  is related to the optical transmission process. Comparison of non-doped synthesized titanium dioxide nanoparticles with commercial titanium dioxide, which has a bandgap of 3.2 eV shows that nanoparticles synthesized by the sol-gel method have a lower bandgap; this difference can be due to the effect of parameters during the synthesis of nanoparticles. Therefore, it can be reported that nanoparticles synthesized by the sol-gel method have better catalytic properties than commercial titanium dioxide [42]. According to Fig. 5, iron doping and magnetization of titanium dioxide caused the absorption wavelength to shift to larger wavelengths and get closer to the visible region. The reduction in bandgap is also due to the action of 3d orbital of titanium and the d orbital of iron, and the placement of iron in the structure of titanium dioxide as an intermediate between titanium dioxide atoms leads to the production of an extra energy level between the valence and the conduction bands of titanium oxide. In fact, the doped iron element in the structure of titanium dioxide acts as an intermediate energy level, reducing the bandgap and changing the absorption of light towards the visible region [24]. On the other hand, by doping the elements to the structure of titanium dioxide, its bandgap is reduced to 2.7 and 2.4 in 2% molar

Table 1  
Mass percentage of elements in nanoparticles synthesized using EDX analysis

Sample elements	Fe <sub>3</sub> O <sub>4</sub>	Fe-doped TiO <sub>2</sub>	Fe-doped TiO <sub>2</sub> @Fe <sub>3</sub> O <sub>4</sub>
O	11.1	21.7	36.9
Ti	–	72.1	60.8
Fe	88.9	6.2	2.3
Total	100	100	100

Table 2  
Surface porosity and specific surface area of synthesized nanoparticles

Nanocatalyst	S <sub>BET</sub> (m <sup>2</sup> /g)	Total pore volume ( $p/p_0 = 0.990$ ) (cm <sup>3</sup> /g)	Average pore diameter (nm)
Fe <sub>3</sub> O <sub>4</sub>	74.405	0.064	3.468
Fe-doped TiO <sub>2</sub>	112.96	0.195	6.905
Fe-doped TiO <sub>2</sub> @Fe <sub>3</sub> O <sub>4</sub>	68.993	0.097	5.668

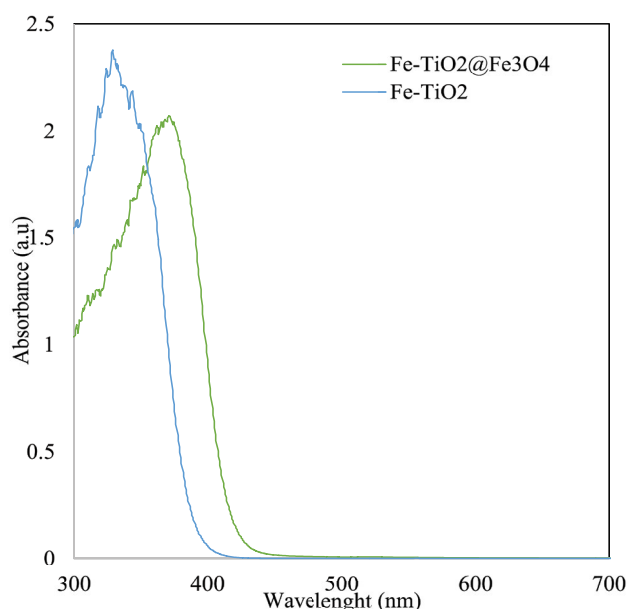


Fig. 5. UV-Vis DRS spectra of Fe-doped TiO<sub>2</sub> and Fe-doped TiO<sub>2</sub>@Fe<sub>3</sub>O<sub>4</sub> samples.

Fe-TiO<sub>2</sub> and Fe-TiO<sub>2</sub>@Fe<sub>3</sub>O<sub>4</sub> samples, respectively. The reduction in bandgap in iron-doped titanium dioxide can be due to iron doping in the structure of titanium dioxide [22].

### 3.1.6. BET analysis

BET analysis was performed using the Belsorp mini apparatus (made in Japan) according to the standard 15901-2. The results of nitrogen adsorption–desorption isotherms for Fe<sub>3</sub>O<sub>4</sub>, Fe-doped TiO<sub>2</sub> and Fe-doped TiO<sub>2</sub>@Fe<sub>3</sub>O<sub>4</sub> samples are shown in Fig. 6a–c. The surface porosity and specific surface area of the samples synthesized using BET analysis are presented in Table 2. As can be seen, based on the classification of the IUPAC standards, the samples evaluated in this study have type IV isotherms

that indicate the simultaneous presence of micropores and mesopores in the synthesized sample. On the other hand, in the adsorption–desorption diagram,  $p/p_0$  below 0.5 is connected, which indicates the simultaneous existence of micropores and mesopores. According to the hysteresis absorption and desorption curves, as well as according to the standard 15901-2, the shape of the pores is often cylindrical. In addition, the total pore volume and average pore diameter in the synthesized Fe<sub>3</sub>O<sub>4</sub>, Fe-TiO<sub>2</sub> and Fe-TiO<sub>2</sub>@Fe<sub>3</sub>O<sub>4</sub> samples are presented in Table 2. It can be seen that in doped and magnetized samples, the amount of specific surface area has decreased, which can be due to the increase in particle size and the resulting blockage of cavities [43].

### 3.1.7. VSM analysis

Vibrating sample magnetometer (VSM) was used to measure the magnetic properties of the synthesized nanoparticles. Fig. 7 shows the magnetic properties of Fe<sub>3</sub>O<sub>4</sub> and Fe-doped TiO<sub>2</sub>@Fe<sub>3</sub>O<sub>4</sub> nanoparticles. As shown, the maximum saturation magnet for Fe<sub>3</sub>O<sub>4</sub> and Fe-TiO<sub>2</sub>@Fe<sub>3</sub>O<sub>4</sub> nanoparticles is about ±80% and ±60%, respectively. The data show that all samples have superparamagnetic properties. For isolation and reuse of the samples, magnetic nanoparticles that exhibit superparamagnetic behavior at room temperature are preferred.

## 3.2. Process of photocatalytic degradation of erythromycin

### 3.2.1. Effect of initial pH of solution

Fig. 8 shows the effect of pH on the erythromycin degradation process at different levels of acid, neutral, and alkali at different times by keeping other variables constant. As shown in Fig. 8, pH = 5 had the highest efficiency and at alkaline and neutral pHs, the removal efficiency decreased. Determining the effect of pH on the degradation of pollutants is a complex matter and depends on several factors: (i) the equilibrium of water decomposition that affects the amount of hydroxyl

Table 3  
Effect of different variables on the degradation of the antibiotic erythromycin

Parameter	Value of variable	Equation	$k_0 \times 10^{-2} \text{ (min}^{-1}\text{)}$	$R^2$	$t_{1/2} \text{ (min)}^*$
Initial pH	3	$y = 0.0283x + 0.0185$	2.83	0.99	24.48
	5	$y = 0.0293x + 0.1092$	2.93	0.96	23.65
	7	$y = 0.0155x + 0.0739$	1.55	0.97	44.70
	9	$y = 0.0116x + 0.0469$	1.16	0.97	59.74
Ciprofloxacin (mg/L)	25	$y = 0.0387x + 0.0656$	3.87	0.98	17.90
	50	$y = 0.0293x + 0.1092$	2.93	0.96	23.65
	75	$y = 0.024x + 0.0126$	2.4	0.99	28.87
Fe-doped TiO <sub>2</sub> (mg/L)	200	$y = 0.026x + 0.0234$	2.6	0.99	26.65
	400	$y = 0.0393x - 0.0056$	3.93	0.99	17.63
	600	$y = 0.0818x - 0.3987$	8.18	0.95	8.47

\* $t_{1/2} \text{ (min)} = 0.693/k_0$

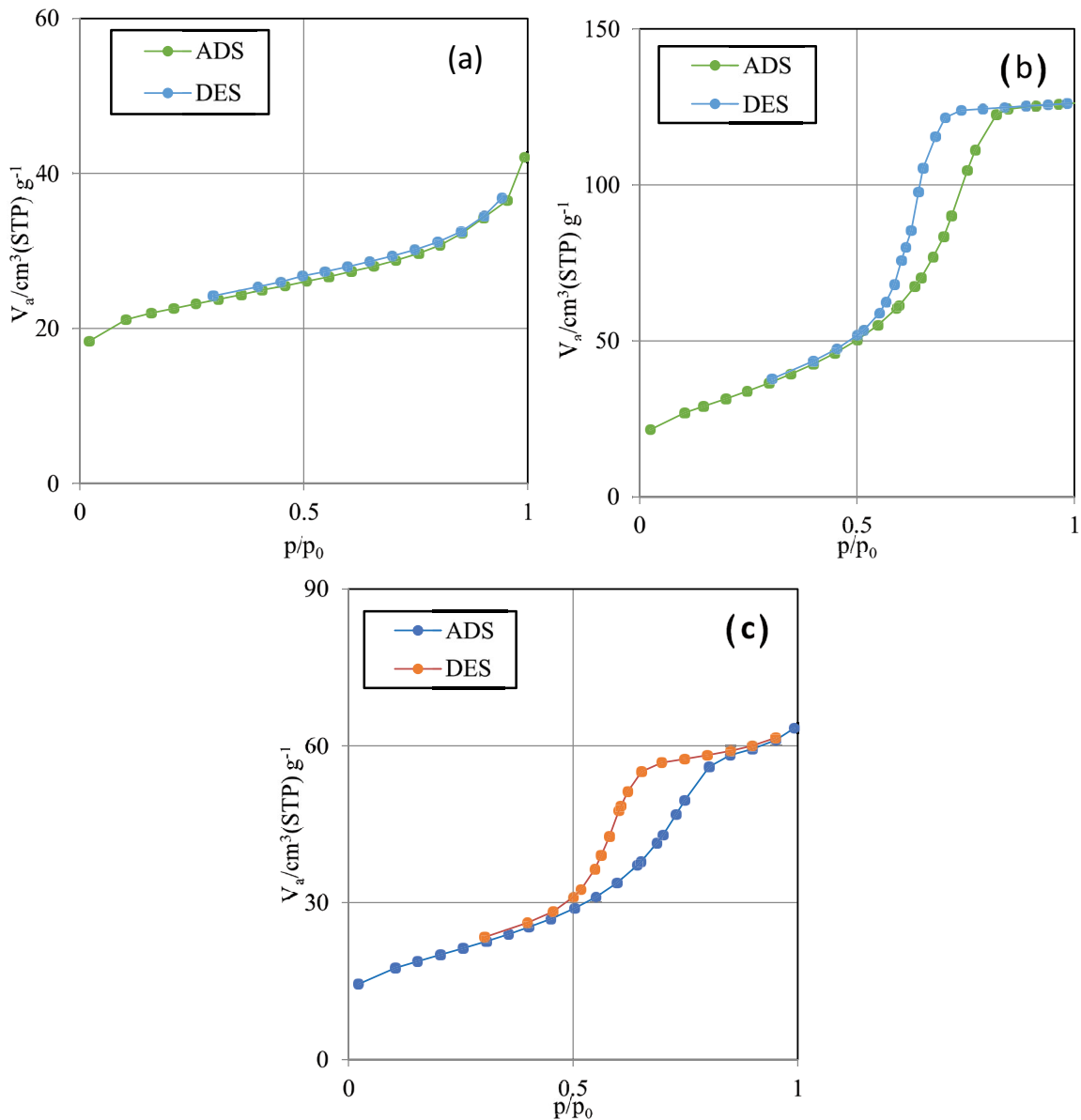


Fig. 6. Nitrogen adsorption–desorption isotherms (a)  $\text{Fe}_3\text{O}_4$ , (b) Fe-doped  $\text{TiO}_2$  and (c) Fe-doped  $\text{TiO}_2 @ \text{Fe}_3\text{O}_4$ .



radicals produced, (ii) the surface charge of the catalyst with respect to the zero charge point (pzc), (iii) ionization state of erythromycin (pKa is 8.8) and its degradation products (iv) the power and oxidation power of the produced optical cavities. At pH less than 6.2 which is the pzc of titania nanoparticles, the charge of the catalyst surface is positive while at pH more than 6.2, the catalyst surface charge is negative. Therefore, at pH = 5 the catalyst levels and erythromycin both have a positive charge and cause a repulsive force, it cannot be proved with pzc and zeta potential. Given that the activity of optical cavities produced under acidic conditions is favorable, while hydroxyl radicals are the predominant species under alkaline and neutral conditions, this may explain the rapid degradation of erythromycin at low pH values. In addition, assuming that the degradation products of erythromycin are negatively charged mainly, it increases the electrostatic attraction forces between the organic matter and the catalyst surface [23,29]. In a study by Li et al. [44] entitled photocatalytic degradation of erythromycin tetracycline using nanocomposite, the optimum pH for erythromycin removal was 5. This may be due to the fact that most erythromycin degradation products have a negative charge, so acidic conditions are suitable for electrostatic attraction between the organic material and the catalyst surface.

### 3.2.2. Effect of initial erythromycin concentration

After determining the optimal pH, the effect of different concentrations of erythromycin (25, 50, and 75 mg/L) on the removal efficiency was investigated at this stage and its results were publicized in Fig. 9. As indicated by the results, the highest efficiency occurs at the less initial concentration and decreases with increasing contaminant concentration. The results of the present study were consistent with the results of the study conducted by Xekoukoulotakis et al. [45] for the photocatalytic degradation of erythromycin. In the mentioned study, with increasing the concentration from 2.5 to 30 mg/L, the efficiency decreased from 77.65% to 19%.

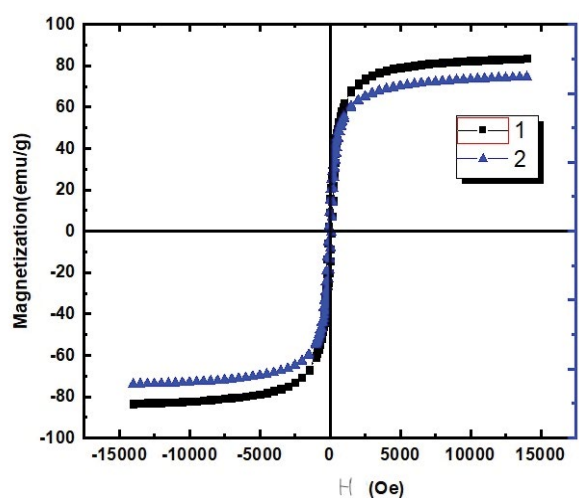


Fig. 7. Magnetic properties of synthesized nanoparticles (1)  $\text{Fe}_3\text{O}_4$  sample and (2) Fe-doped  $\text{TiO}_2@ \text{Fe}_3\text{O}_4$  sample.

The reason for the decrease in efficiency with increasing concentration can be due to reduced amount of reactive species (such as hydroxyl radical, etc.) for the degradation of the target pollutant, more competition for reactive species between the target pollutant and the intermediate products of degradation with increasing pollutant concentration, competition between contaminant molecules for high hydroxyl

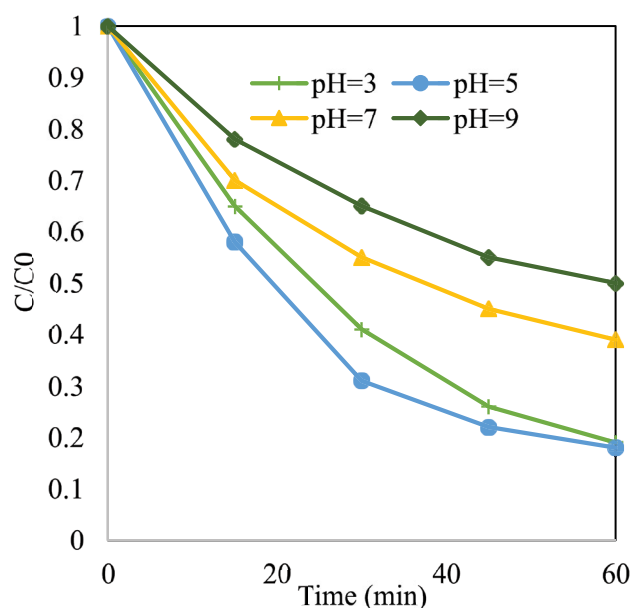


Fig. 8. Effect of initial pH on photocatalytic removal of erythromycin (initial concentration of erythromycin: 50 mg/L, catalyst concentration: 400 mg/L).

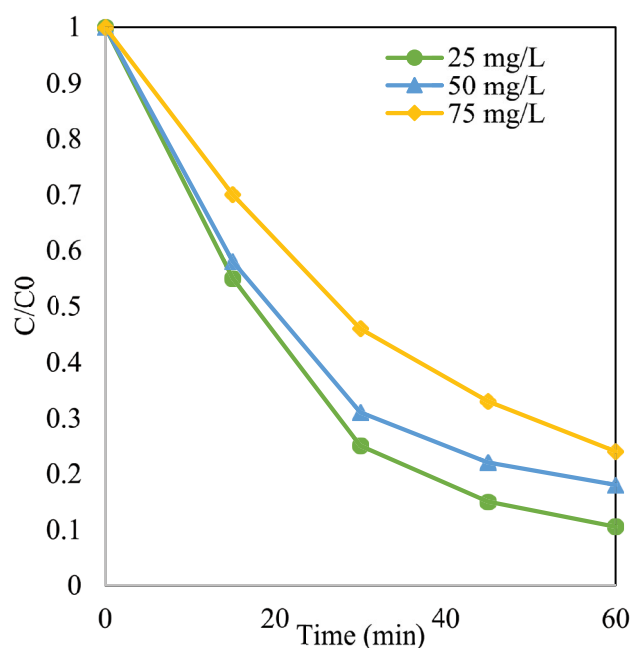


Fig. 9. Effect of initial erythromycin concentration on photocatalytic removal of erythromycin (pH of 5 and catalyst concentration of 400 mg/L).

radicals at high concentrations and blocking of active catalyst sites by intermediate and contaminant compounds [46,47]. In their study, Mohammadi et al. [48] showed that with increasing contaminant concentration, more contaminant molecules adhere to the catalyst surface, and the active sites of the catalyst decrease; therefore, with the increase of the occupied sites of the catalyst surface, the formation of hydroxyl radicals decreases. Sohrabnejad et al. [49] showed that increasing the concentration of the pollutant can reduce the number of photons that reach the surface of the catalyst because the higher absorption of light by the pollutant, leads to more decrease in the stimulation of the catalysts and consequently, reduce the production of hydroxyl radicals.

### 3.2.3. Effect of different amounts of catalyst

One of the most important parameters affecting the efficiency and performance of hybrid processes and catalytic oxidation is the catalyst dosage used in the process. Fig. 10 shows the effect of different doses of synthesized nanoparticles (200, 400, and 600 mg/L) on the removal of erythromycin. According to the figure, with increasing catalyst dosage, the removal efficiency has increased. The study of Fakhri et al. [50] conducted for the photocatalytic degradation of erythromycin showed that by increasing the nanocatalyst dosage from 300 to 500 mg/L, the efficiency of the process increases. They reported that the reason for this phenomenon could be that as the nanocatalyst dosage increases, the number of active sites at the nanocatalyst surface increases, and more erythromycin molecules are adsorbed on the nanocatalyst surface. On the other hand, increasing the nanocatalyst dosage and active sites leads to the formation of more hydroxyl radicals

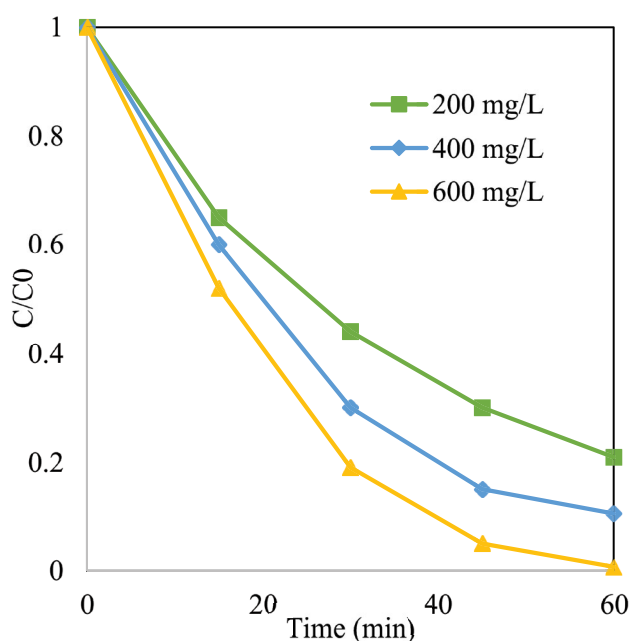


Fig. 10. Effect of different dosage of nanoparticles on photocatalytic removal of erythromycin (pH 5 and initial erythromycin concentration: 25 mg/L).

and increases the photocatalytic activity [50]. The results of the study by Guo et al. [51] performed for the degradation of Flumequine using plasma along with graphene oxide/titanium dioxide nanocomposite showed that by increasing the catalyst dosage, the contact surface and catalytic reaction are improved and more photons are produced and converted into energy by the plasma process, which accelerates the catalytic process.

### 3.3. Reaction kinetics

The removal kinetics of many contaminants have been analyzed using a first-order kinetic model, and this model is used to express the relationship between the contaminant degradation rate in photocatalytic degradation reactions. The first order kinetic equation is as follows:

$$r = -\frac{dc}{dt} = k_{\text{obs}} C \quad (3)$$

where  $r$  (mg/L min) is photocatalytic degradation rate of erythromycin antibiotic in the initial reaction times,  $C = C_0$  (mg/L) is initial concentration of erythromycin antibiotic, and  $k_{\text{obs}}$  (L/mg) is the erythromycin degradation rate constant, which is affected by the concentration of antibiotics. In cases where the chemical concentration is low ( $C = C_0$  at  $t = 0$ ), the equation becomes simpler and is used as a first-order equation represented as follows:

$$\ln\left(\frac{C_0}{C_t}\right) = k_{\text{obs}} t \quad (4)$$

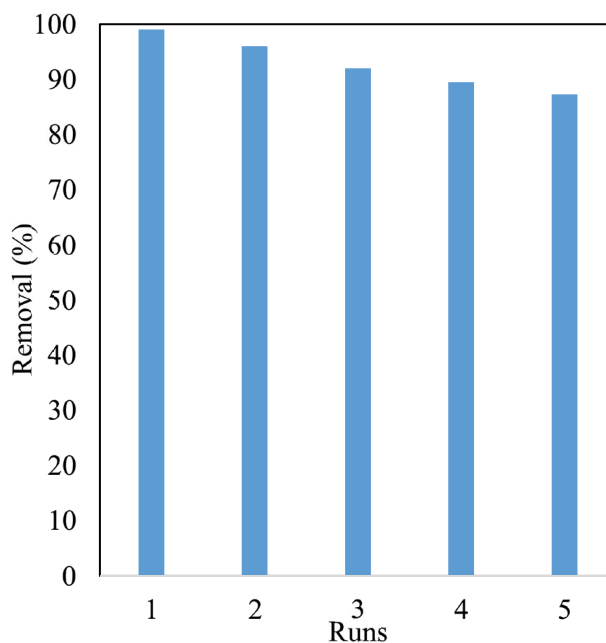


Fig. 11. Evaluation of reusability of synthesized nanocatalysts under optimal conditions for removal of erythromycin antibiotic.

By plotting  $\ln(C_0/C_t)$  against time at different concentrations of antibiotics, the amount of  $k_{obs}$  and the correlation coefficient can be determined for different concentrations. The apparent velocity constant of first-order kinetics ( $k_{obs}$ ) is equal to the slope of the line. According to the above, the effect of various parameters including the initial concentration of antibiotics, solution pH, and dose of magnetic nanoparticles on the degradation kinetics of antibiotics was investigated. Table 3 presents the regression coefficient ( $R^2$ ), the first-order reaction rate constant of various parameters, and the half-life of the reaction, which is the time required to reduce the reaction concentration. The high regression coefficient of the parameters in Table 3 shows that the photocatalytic degradation of the antibiotic follows the first-order kinetic model well. The results showed that the absorption is done in the one step.

### 3.4. Assessment of sustainability and reuse

The reusability of the synthesized nanocatalysts after the oxidation steps was investigated under optimal conditions. Photocatalyst, after several separations and washes, was dried at 60°C. Fig. 11 shows that the degradation efficiency of the erythromycin photocatalytic process after 5 consecutive repetitions is 99.03%, 96%, 92%, 89.5%, and 87.25%. As can be seen, the reduction in efficiency after reuse is small and can be due to leaching of iron ions, loss of active sites during the degradation process or poisoning of the catalyst surface by adsorption of intermediates produced in the photocatalytic process. In the studies by Alborno et al. [18] and Mugunthan et al. [52], they attributed the reduction in degradation efficiency to the poisoning of the catalyst surface with the by-products produced. Evidence suggests that doped and synthesized magnetic photocatalysts have reasonable catalytic stability and relatively small reductions in catalytic activity for antibiotic degradation. Therefore, the catalyst synthesized in the present study is proposed as a stable and efficient photocatalyst for real applications in the future.

### 3.5. Antibiotic decomposition products

The complex structure of erythromycin contains 14 loops of lactone, cladinose sugars, and desosamine deoxy sugar, and its molecular formula is  $C_{37}H_{67}O_{13}N$  and its molecular weight is 733 g/mol. By removing the sugars cladinose and desosamine deoxy and separating the lactone ring, products with molecular weights of 176, 175 and 382 are produced, respectively. Another pathway for degradation involves the attack of a radical ion on the lactone ring and the production of a deprotonated product with a molecular weight of 690, which was further degraded to deprotonated intermediaries of 587, 471, 439, 293, and protonated products of 491 m/z. The degradation products and their molecular weights were reported in Table 4 [53]. According to a study by Luiz et al. [54], the degradation of erythromycin by hydroxyl radical begins with the abduction of hydrogen. erythromycin is a saturated organic compound containing 13 oxygen atoms, which falls into the functional groups of 1 ester, 1 carbonyl (ketone class), 5 ether and 5 hydroxyl groups (alcohol class). As a result,

the major degradation pathways due to hydrogen capture during the reaction of hydroxyl radical and saturated organic compounds in the presence of oxygen will be the shortening of the chains of ketones, aldehydes and carboxylic acids. In the treatment using hydroxyl radicals, fewer initial degradation products were observed compared to in ozone treatment, probably because the reaction of hydroxyl radicals is non-selective.

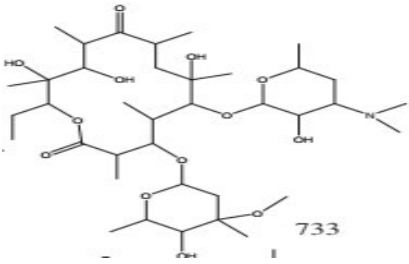
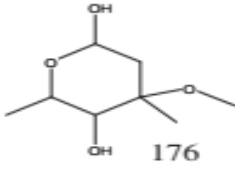
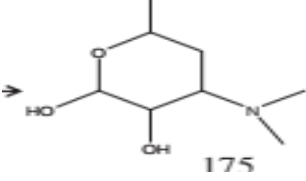
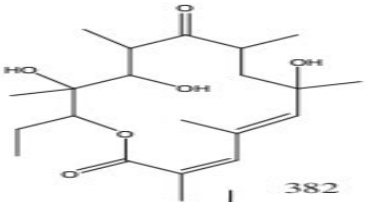
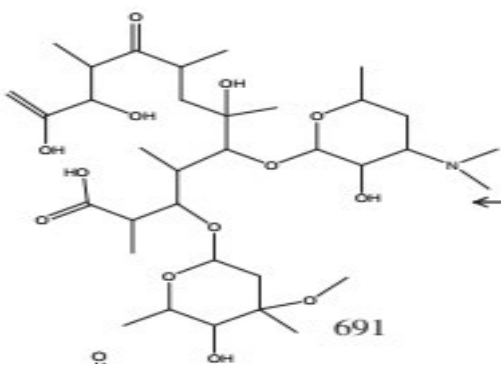
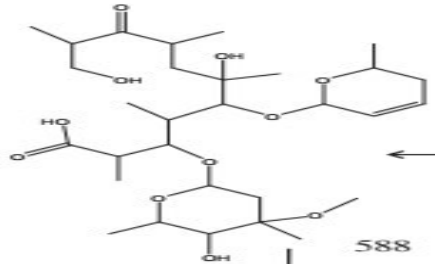
## 4. Conclusion

This study was performed to evaluate the photocatalytic oxidation efficiency of erythromycin from aqueous media by iron-doped titanium dioxide magnetic nanoparticles. In this study, the effect of various parameters such as pH, initial concentration of erythromycin, and dose of synthesized nanoparticles was investigated. Fe-doped  $TiO_2@Fe_3O_4$  nanoparticles were synthesized by sol-gel method, and SEM, EDX, FTIR, XRD, VSM, BET and DRS analyses were used to determine the properties of the synthesized nanoparticles. Various analyses of the synthesized nanoparticles showed that the nanoparticles have good uniformity and dispersion. The surface morphology of the nanoparticles showed that these particles tended to accumulate. In XRD analysis, the formation of large and sharp peaks confirmed the good crystal structure of the synthesized nanoparticles. In FTIR analysis, the presence of more hydroxyl and water groups in the Fe-doped  $TiO_2@Fe_3O_4$  sample leads to increase the activity of photocatalytic processes. Strong Ti and O signals in the EDX spectrum indicate that  $TiO_2$  surrounds  $Fe_3O_4$  with a core-shell structure. In doped and magnetized samples, the amount of specific surface area has decreased, which can be due to the increase in particle size and the resulting blockage of cavities. Data from VSM analysis showed that all samples have superparamagnetic properties. The photocatalytic degradation of antibiotic follows the first-order kinetic model well. Doped and synthesized magnetic photocatalysts have reasonable catalytic stability and relatively small reductions in catalytic activity for antibiotic degradation. The doping of iron in the structure of titanium dioxide caused the absorption wavelength to shift to higher wavelengths and get closer to the visible region. The maximum removal efficiencies of erythromycin were obtained using a 15-W UVC lamp under optimal conditions including pH of 5, initial concentration of 25 mg/L, and catalyst dosage of 600 mg/L at a reaction time of 60 min. Therefore, due to the high efficiency of the photocatalytic process, the use of this process is recommended in complementary water and wastewater treatment processes to remove erythromycin.

## Acknowledgment

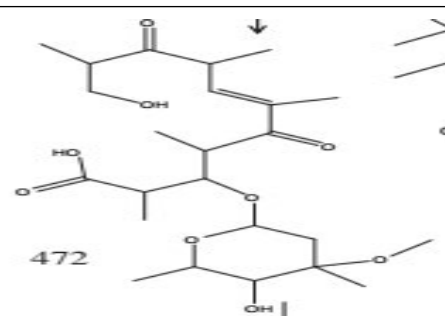
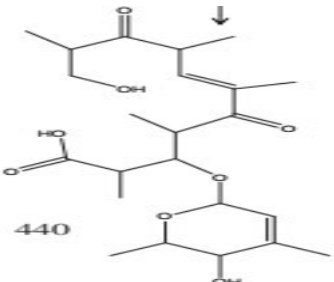
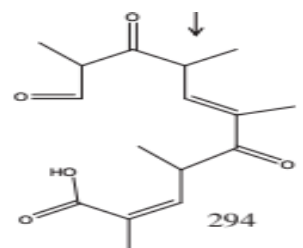
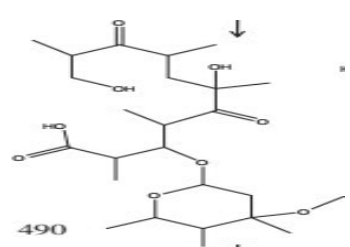
This article is the result of a part of the Ph.D. Thesis entitled "Evaluation of the photocatalytic removal efficiency of erythromycin using magnetic nanoparticles (Fe-doped  $TiO_2@Fe_3O_4$ ) from aqueous solutions", which has been supported by Islamic Azad University, Science and Research Branch of Tehran. We would like to thank the Islamic Azad University for its financial support of this research.

Table 4  
Determined photodegradation products of erythromycin in the study of Kamani et al. [46]

Products	Molecular weight	Proposed structure
Erythromycin	733	
Product 1	176	
Product 2	175	
Product 3	382	
Product 4	691	
Product 5	588	

(Continued)

Table 4 Continued

Products	Molecular weight	Proposed structure
Product 6	472	
Product 7	440	
Product 8	294	
Product 9	490	

### Conflicts of interest/Competing interests

The authors declare that they have no competing interests.

### References

- [1] D. Dimitrakopoulou, I. Rethemiotaki, Z. Frontistis, N.P. Xekoukoulotakis, D. Venieri, D. Mantzavinos, Degradation, mineralization and antibiotic inactivation of amoxicillin by UV-A/TiO<sub>2</sub> photocatalysis, *J. Environ. Manage.*, 98 (2012) 168–174.
- [2] A. Fakhri, S. Adami, Adsorption and thermodynamic study of Cephalosporins antibiotics from aqueous solution onto MgO nanoparticles, *J. Taiwan Inst. Chem. Eng.*, 45 (2014) 1001–1006.
- [3] H. Liu, W. Liu, J. Zhang, C. Zhang, L. Ren, Y. Li, Removal of cephalaxin from aqueous solutions by original and Cu(II)/Fe(III) impregnated activated carbons developed from lotus stalks kinetics and equilibrium studies, *J. Hazard. Mater.*, 185 (2011) 1528–1535.
- [4] M. Fazlzadeh, S. Gulshan, A. Bohloul, M. Rezaei, Evaluation of electro-Fenton process in amoxicillin removal from aqueous solutions, *J. Health Hyg.*, 7 (2016) 276–287.
- [5] Y.J. Jung, W.G. Kim, Y. Yoon, J.-W. Kang, Y.M. Hong, H.W. Kim, Removal of amoxicillin by UV and UV/H<sub>2</sub>O<sub>2</sub> processes, *Sci. Total Environ.*, 420 (2012) 160–167.
- [6] T.C. Morris, L. Ranaghan, J. Morrison, Phase II trial of clarithromycin and pamidronate therapy in myeloma, *Med. Oncol.*, 18 (2001) 79–84.
- [7] J. Kadota, H. Mukae, H. Ishii, T. Nagata, H. Kaida, K. Tomono, S. Kohno, Long-term efficacy and safety of clarithromycin treatment in patients with diffuse panbronchiolitis, *Respir. Med.*, 97 (2003) 844–850.
- [8] F. Javier Benitez, J.L. Acero, F.J. Real, G. Roldán, E. Rodriguez, Ultrafiltration and nanofiltration membranes applied to the removal of the pharmaceuticals amoxicillin, naproxen, metoprolol and phenacetin from water, *J. Chem. Technol. Biotechnol.*, 86 (2011) 858–866.
- [9] Z. Heidari, R. Pelalak, R. Eshaghi Malekshah, M. Pishnamazi, M. Rezakazemi, T.M. Aminabhavi, S. Shirazian, A new insight

- into catalytic ozonation of sulfasalazine antibiotic by plasma-treated limonite nanostructures: experimental, modeling and mechanism, *Chem. Eng. J.*, 428 (2022) 131230, doi: 10.1016/j.cej.2021.131230.
- [10] G. Yang, Y. Liang, Z. Xiong, J. Yang, K. Wang, Z. Zeng, Molten salt-assisted synthesis of  $\text{Ce}_4\text{O}_7/\text{Bi}_4\text{MoO}_9$  heterojunction photocatalysts for photo-Fenton degradation of tetracycline: enhanced mechanism, degradation pathway and products toxicity assessment, *Chem. Eng. J.*, 425 (2021) 130689, doi: 10.1016/j.cej.2021.130689.
- [11] K. Hasani, A. Peyghami, A. Moharrami, M. Vosoughi, A. Dargahi, The efficacy of sono-electro-Fenton process for removal of cefixime antibiotic from aqueous solutions by response surface methodology (RSM) and evaluation of toxicity of effluent by microorganisms, *Arabian J. Chem.*, 13 (2020) 6122–6139.
- [12] Q. Shang, W. Chi, P. Zhang, Y. Ling, X. Liu, G. Cui, W. Liu, X. Shi, B. Tang, Optimization of  $\text{Bi}_2\text{O}_3/\text{TS-1}$  preparation and photocatalytic reaction conditions for low concentration erythromycin wastewater treatment based on artificial neural network, *Process Saf. Environ. Prot.*, 157 (2022) 297–305.
- [13] H. Mahmoodi, M. Fattahi, M. Motevassel, Graphene oxide-chitosan hydrogel for adsorptive removal of diclofenac from aqueous solution: preparation, characterization, kinetic and thermodynamic modelling, *RSC Adv.*, 11 (2021) 36289–36304.
- [14] C. Brahmī, M. Benlifa, M. Ghali, F. Dumur, C. Simonnet-Jégat, M. Valérie, F. Morlet-Savary, L. Bousselmi, J. Lalevée, Performance improvement of the photocatalytic process for the degradation of pharmaceutical compounds using new POM/polymer photocatalysts, *J. Environ. Chem. Eng.*, 9 (2021) 106015, doi: 10.1016/j.jece.2021.106015.
- [15] J. Ma, F. Zhu, P. Ji, Q. Zou, H. Wang, G. Xu, Enhanced visible-light photocatalytic performance of Co/Ni doped  $\text{Cu}_2\text{MoS}_4$  nanosheets for Rhodamine B and erythromycin degradation, *J. Alloys Compd.*, 863 (2021) 158612, doi: 10.1016/j.jallcom.2021.158612.
- [16] S. Su, W. Guo, C. Yi, Y. Leng, Z. Ma, Degradation of amoxicillin in aqueous solution using sulphate radicals under ultrasound irradiation, *Ultrason. Sonochem.*, 19 (2012) 469–474.
- [17] R. Kidak, Ş. Doğan, Medium-high frequency ultrasound and ozone based advanced oxidation for amoxicillin removal in water, *Ultrason. Sonochem.*, 40 (2018) 131–139.
- [18] L.L. Albornoz, S.W. da Silva, J.P. Bortolozzi, E.D. Banús, P. Brussino, M.A. Ulla, A.M. Bernardes, Degradation and mineralization of erythromycin by heterogeneous photocatalysis using  $\text{SnO}_2$ -doped  $\text{TiO}_2$  structured catalysts: activity and stability, *Chemosphere*, 268 (2021) 128858, doi: 10.1016/j.chemosphere.2020.128858.
- [19] M. Sui, S. Xing, L. Sheng, S. Huang, H. Guo, Heterogeneous catalytic ozonation of ciprofloxacin in water with carbon nanotube supported manganese oxides as catalyst, *J. Hazard. Mater.*, 227–228 (2012) 227–236.
- [20] H. Asadzadeh Patehkor, M. Fattahi, M. Khosravi-Nikou, Synthesis and characterization of ternary chitosan- $\text{TiO}_2$ -ZnO over graphene for photocatalytic degradation of tetracycline from pharmaceutical wastewater, *Sci. Rep.*, 11 (2021) 24177, doi: 10.1038/s41598-021-03492-5.
- [21] A. Garmroudi, M. Kheirollahi, S.A. Mousavi, M. Fattahi, E.H. Mahvelati, Effects of graphene oxide/ $\text{TiO}_2$  nanocomposite, graphene oxide nanosheets and Cedr extraction solution on IFT reduction and ultimate oil recovery from a carbonate rock, *Petroleum*, (2020), doi: 10.1016/j.petlm.2020.10.002 (In Press).
- [22] H. Kamani, S. Nasseri, M. Khoobi, R.N. Nodehi, A.H. Mahvi, Sonocatalytic degradation of humic acid by N-doped  $\text{TiO}_2$  nano-particle in aqueous solution, *J. Environ. Health Sci. Eng.*, 14 (2016) 3, doi: 10.1186/s40201-016-0242-2.
- [23] H. Kamani, S.D. Ashrafi, A. Jahantiq, E. Norabadi, M. Dashti Zadeh, Catalytic degradation of humic acid using Fe-doped  $\text{TiO}_2$  - ultrasound hybrid system from aqueous solution, *Int. J. Environ. Anal. Chem.*, (2021) 1–15, doi: 10.1080/03067319.2021.1979535.
- [24] V. Moradi, M.B. Jun, A. Blackburn, R.A. Herring, Significant improvement in visible light photocatalytic activity of Fe-doped  $\text{TiO}_2$  using an acid treatment process, *Appl. Surf. Sci.*, 427 (2018) 791–799.
- [25] D. Panda, S. Manickam, Recent advancements in the sonophotocatalysis (SPC) and doped-sonophotocatalysis (DSPC) for the treatment of recalcitrant hazardous organic water pollutants, *Ultrason. Sonochem.*, 36 (2017) 481–496.
- [26] M. Dashtizadeh, H. Kamani, S.D. Ashrafi, A. Hossein Panahi, A.H. Mahvi, D. Balarak, M. Hoseini, H. Ansari, E. Bazrafshan, F. Parsafar, Human health risk assessment of trace elements in drinking tap water in Zahedan city, Iran, *J. Environ. Health Sci. Eng.*, 17 (2019) 1163–1169.
- [27] A. Hossein Panahi, S.D. Ashrafi, H. Kamani, M. Khodadadi, E. Lima, F.K. Mostafapour, A. Mahvi, Removal of cephalixin from artificial wastewater by mesoporous silica materials using Box-Behnken response surface methodology, *Desal. Water Treat.*, 159 (2019) 169–180.
- [28] A. Jahantiq, R. Ghanbari, A. Hossein Panahi, S.D. Ashrafi, A.D. Khatibi, E. Noorabadi, A. Meshkinian, H. Kamani, Photocatalytic degradation of 2,4,6-trichlorophenol in aqueous solutions using synthesized Fe-doped  $\text{TiO}_2$  nanoparticles via response surface methodology, *Desal. Water Treat.*, 159 183 (2020) 366–373.
- [29] E. Norabadi, S.D. Ashrafi, H. Kamani, A. Jahantiq, Degradation of 2,6-dichlorophenol by Fe-doped  $\text{TiO}_2$  Sonophotocatalytic process: kinetic study, intermediate product, degradation pathway, *Int. J. Environ. Anal. Chem.*, (2020) 1–16, doi: 10.1080/03067319.2020.1837122.
- [30] Z. Es'haghi, A. Nezhadali, A.-D. Khatibi, Magnetically responsive polycaprolactone nanoparticles for progesterone screening in biological and environmental samples using gas chromatography, *Anal. Bioanal. Chem.*, 408 (2016) 5537–5549.
- [31] R. Wang, X. Wang, X. Xi, R. Hu, G. Jiang, Preparation and photocatalytic activity of magnetic  $\text{Fe}_3\text{O}_4/\text{SiO}_2/\text{TiO}_2$  composites, *Adv. Mater. Sci. Eng.*, 2012 (2012) 409379, doi: 10.1155/2012/409379.
- [32] H. Niu, Q. Wang, H. Liang, M. Chen, C. Mao, J. Song, S. Zhang, Y. Gao, C. Chen, Visible-light active and magnetically recyclable nanocomposites for the degradation of organic dye, *Materials*, 7 (2014) 4034–4044.
- [33] C.L. Luu, Q.T. Nguyen, S.T. Ho, Synthesis and characterization of Fe-doped  $\text{TiO}_2$  photocatalyst by the sol-gel method, *Adv. Nat. Sci. Nanosci. Nanotechnol.*, 1 (2010) 015008, doi: 10.1088/2043-6254/1/1/015008.
- [34] E. Craciun, L. Predoana, I. Atkinson, I. Jitaru, E.M. Anghel, V. Bratan, C. Gifu, C. Anastasescu, A. Rusu, V. Raditoiu, E. Vasile, M. Anastasescu, I. Balint, M. Zaharescu,  $\text{Fe}^{3+}$ -doped  $\text{TiO}_2$  nanopowders for photocatalytic mineralization of oxalic acid under solar light irradiation, *J. Photochem. Photobiol., A*, 356 (2018) 18–28.
- [35] S. Hu, A. Wang, X. Li, H. Löwe, Hydrothermal synthesis of well-dispersed ultrafine N-doped  $\text{TiO}_2$  nanoparticles with enhanced photocatalytic activity under visible light, *J. Phys. Chem. Solids*, 71 (2010) 156–162.
- [36] G.-S. Shao, X.-J. Zhang, Z.-Y. Yuan, Preparation and photocatalytic activity of hierarchically mesoporous-macroporous  $\text{TiO}_2$ -N, *Appl. Catal., B*, 82 (2008) 208–218.
- [37] N. Abbas, G.N. Shao, M.S. Haider, S. Imran, S.S. Park, H.T. Kim, Sol-gel synthesis of  $\text{TiO}_2$ - $\text{Fe}_2\text{O}_3$  systems: effects of  $\text{Fe}_2\text{O}_3$  content and their photocatalytic properties, *J. Ind. Eng. Chem.*, 39 (2016) 112–120.
- [38] J. Choi, H. Park, M.R. Hoffmann, Effects of single metal-ion doping on the visible-light photoreactivity of  $\text{TiO}_2$ , *J. Phys. Chem. C*, 114 (2010) 783–792.
- [39] S.B. Eadi, S. Kim, S.W. Jeong, H.W. Jeon, Novel preparation of Fe-doped  $\text{TiO}_2$  nanoparticles and their application for gas sensor and photocatalytic degradation, *Adv. Mater. Sci. Eng.*, 2017 (2017) 2191659, doi: 10.1155/2017/2191659.
- [40] D.R. Reddy, G.K. Dinesh, S. Anandan, T. Sivasankar, Sonophotocatalytic treatment of Naphthol Blue Black dye and real textile wastewater using synthesized Fe-doped  $\text{TiO}_2$ , *Chem. Eng. Process. Process Intensif.*, 99 (2016) 10–18.
- [41] N. Farhangi, R.R. Chowdhury, Y. Medina-Gonzalez, M.B. Ray, P.A. Charpentier, Visible light active Fe-doped  $\text{TiO}_2$  nanowires

- grown on graphene using supercritical CO<sub>2</sub>, *Appl. Catal., B*, 110 (2011) 25–32.
- [42] Y. Sui, Q. Liu, T. Jiang, Y. Guo, Synthesis of nano-TiO<sub>2</sub> photocatalysts with tunable Fe doping concentration from Ti-bearing tailings, *Appl. Surf. Sci.*, 428 (2018) 1149–1158.
- [43] P.M. Álvarez, J. Jaramillo, F. Lopez-Pinero, P.K. Plucinski, Preparation and characterization of magnetic TiO<sub>2</sub> nanoparticles and their utilization for the degradation of emerging pollutants in water, *Appl. Catal., B*, 100 (2010) 338–345.
- [44] G. Li, B. Wang, J. Zhang, R. Wang, H. Liu, Rational construction of a direct Z-scheme g-C<sub>3</sub>N<sub>4</sub>/CdS photocatalyst with enhanced visible light photocatalytic activity and degradation of erythromycin and tetracycline, *Appl. Surf. Sci.*, 478 (2019) 1056–1064.
- [45] N.P. Xekoukoulotakis, N. Xinidis, M. Chroni, D. Mantzavinos, D. Venieri, E. Hapeshi, D. Fatta-Kassinos, UV-A/TiO<sub>2</sub> photocatalytic decomposition of erythromycin in water: factors affecting mineralization and antibiotic activity, *Catal. Today*, 151 (2010) 29–33.
- [46] H. Kamani, G.H. Safari, G. Asgari, S.D. Ashrafi, Data on modeling of enzymatic elimination of Direct Red 81 using response surface methodology, *Data Brief*, 18 (2018) 80–86.
- [47] E. Norabadi, A. Hossein Panahi, R. Ghanbari, A. Meshkinian, H. Kamani, S.D. Ashrafi, Optimizing the parameters of amoxicillin removal in a photocatalysis/ozonation process using Box–Behnken response surface methodology, *Desal. Water Treat.*, 192 (2020) 234–240.
- [48] R. Mohammadi, B. Massoumi, M. Rabani, Photocatalytic decomposition of amoxicillin trihydrate antibiotic in aqueous solutions under UV irradiation using Sn/TiO<sub>2</sub> nanoparticles, *Int. J. Photoenergy*, 2012 (2012) 514856, doi: 10.1155/2012/514856.
- [49] S. Sohrabnezhad, Study of catalytic reduction and photo-degradation of methylene blue by heterogeneous catalyst, *Spectrochim. Acta, Part A*, 81 (2011) 228–235.
- [50] A. Fakhri, S. Rashidi, I. Tyagi, S. Agarwal, V.K. Gupta, Photodegradation of erythromycin antibiotic by  $\gamma$ -Fe<sub>2</sub>O<sub>3</sub>/SiO<sub>2</sub> nanocomposite: response surface methodology modeling and optimization, *J. Mol. Liq.*, 214 (2016) 378–383.
- [51] H. Guo, N. Jiang, H. Wang, K. Shang, N. Lu, J. Li, Y. Wu, Degradation of flumequine in water by pulsed discharge plasma coupled with reduced graphene oxide/TiO<sub>2</sub> nanocomposites, *Sep. Purif. Technol.*, 218 (2019) 206–216.
- [52] E. Mugunthan, M.B. Saidutta, P.E. Jagadeeshbabu, Photocatalytic degradation of diclofenac using TiO<sub>2</sub>-SnO<sub>2</sub> mixed oxide catalysts, *Environ. Technol.*, 40 (2019) 929–941.
- [53] B. Gao, S. Dong, J. Liu, L. Liu, Q. Feng, N. Tan, T. Liu, L. Bo, L. Wang, Identification of intermediates and transformation pathways derived from photocatalytic degradation of five antibiotics on ZnIn<sub>2</sub>S<sub>4</sub>, *Chem. Eng. J.*, 304 (2016) 826–840.
- [54] D.B. Luiz, A.K. Genena, E. Virmond, H.J. José, R.F.P.M. Moreira, W. Gebhardt, H. Fr Schröder, Identification of degradation products of erythromycin A arising from ozone and advanced oxidation process treatment, *Water Environ. Res.*, 82 (2010) 797–805.